Microscopy AND
Microanalysis

Original Article

Retarding Field Integrated Fluorescence and Electron Microscope

Yoram Vos[1], Ryan I. Lane[1], Chris J. Peddie[2], Anouk H.G. Wolters[3] and Jacob P. Hoogenboom[1]*

[1]Faculty of Applied Sciences, Delft University of Technology, Lorentzweg 1, Delft 2628CJ, The Netherlands; [2]Electron Microscopy STP, The Francis Crick Institute, 1 Midland Road, London NW1 1AT, UK and [3]Department of Cell Biology, University Medical Center Groningen, University of Groningen, A. Deusinglaan 1, Groningen 9713 AV, The Netherlands

Abstract

The authors present the application of a retarding field between the electron objective lens and sample in an integrated fluorescence and electron microscope. The retarding field enhances signal collection and signal strength in the electron microscope. This is beneficial for samples prepared for integrated fluorescence and electron microscopy as the amount of staining material added to enhance electron microscopy signal is typically lower compared to conventional samples in order to preserve fluorescence. We demonstrate signal enhancement through the applied retarding field for both 80-nm post-embedding immunolabeled sections and 100-nm in-resin preserved fluorescence sections. Moreover, we show that tuning the electron landing energy particularly improves imaging conditions for ultra-thin (50 nm) sections, where optimization of both retarding field and interaction volume contribute to the signal improvement. Finally, we show that our integrated retarding field setup allows landing energies down to a few electron volts with 0.3 eV dispersion, which opens new prospects for assessing electron beam induced damage by *in situ* quantification of the observed bleaching of the fluorescence following irradiation.

Key words: backscattered electron detection, correlative light and electron microscopy, electron beam induced damage, retarding field, SEM

Introduction

Many different forms of hybrid or integrated light and electron microscopes, which combine the strengths of two different types of microscopy into a single apparatus, have been introduced in recent years (Timmermans & Otto, 2015). The main purpose of these microscopes is to facilitate the process of correlating data obtained with the two modalities (Agronskaia et al., 2008; Liv et al., 2013; De Boer et al., 2015; Ando et al., 2018). Alternatively, integrated microscopes can be used to enable new microscopy techniques that can circumvent limitations of either of the stand-alone techniques (Nawa et al., 2014; Bischak et al., 2015). A third potential use of integrated microscopes, which so far has received only little attention, is to use the integrated light microscope to *in situ* monitor sample changes induced by the electron microscope (Nagayama et al., 2016; Yuan et al., 2016).

In many cases, the integration puts restrictions on the capabilities of one of the integrated modalities as compared to a stand-alone system. We have previously presented an integrated system with fluorescence and scanning electron microscopy (SEM) that, in contrast to several integrated modalities, maintains many of the key characteristics of the stand-alone microscopes. These include high-resolution and magnetic immersion SEM, high numerical aperture

fluorescence microscopy (FM) (Timmermans & Otto, 2015), flexibility in fluorescence excitation and detection schemes (Narváez et al., 2014; Moerland et al., 2016; Garming et al., 2017) including super-resolution (Peddie et al., 2017; Pinotsi et al., 2019), a wide choice of EM detectors, and the possibility of using microfluidic enclosures for observing samples in liquid (Liv et al., 2016). However, the use of electrostatic immersion, the application of a retarding or deceleration field between electron objective lens and sample, has so far not been demonstrated in an integrated microscope. Nevertheless, as we will detail below, the application of a retarding electrostatic field may have several key advantages, both for integrated correlative light and electron microscopy (CLEM) and for studying electron-matter interactions with *in situ* light microscopy.

In SEM, a retarding field may be applied for several reasons. In low energy (<10 keV) microscopy, electron deceleration is particularly useful as it allows for higher resolution imaging relative to when the primary beam is brought to its final energy as it exits the objective lens (Müllerová & Frank, 1994). For biological specimens, such as 100 nm or thinner tissue sections, this is particularly important as low energies (1–5 keV) are typically preferred to optimize the electron interaction volume to the thickness of the sample. Also, the electron landing energy may be tuned to selectively image at a specific depth in the sample, instead of the entire depth of the tissue section (Boughorbel, 2012; De Goede et al., 2017). Another advantage of a retarding field is the acceleration of signal electrons toward detectors underneath the objective lens or in the electron column, which may improve

*Author for correspondence: Jacob P. Hoogenboom, E-mail: j.p.hoogenboom@tudelft.nl

CrossMark

signal collection or allow discrimination between different signals (Ohta et al., 2012; Bouwer et al., 2017). For (integrated) CLEM, this could be particularly beneficial as the EM contrast in samples prepared for CLEM is typically weaker compared to conventional EM sample preparation due to, for example, the lack of on section post-staining or reduced concentrations of osmium in order to preserve fluorescence (Watanabe et al., 2011; Peddie et al., 2014a; De Boer et al., 2015). Osmium is used as a fixative and staining agent in biological EM, but it also quenches fluorescence (Karreman et al., 2009, 2012). By improving signal collection, a retarding field could thus help improve signal and contrast in CLEM for samples that have been weakly stained in order to preserve fluorescence.

An additional reason why a retarding field integrated microscope may be beneficial relates to a potential new technique for observing and understanding electron-matter interactions. In CLEM, it is well known that electron beam exposure leads to rapid loss, or bleaching, of fluorescence due to destruction of the organic fluorescent molecules. Therefore, in a CLEM experiment, fluorescence microscopy is always conducted prior to electron microscopy investigation. In addition, electron beam irradiation of organic materials leads to cross-linking, which can in turn induce electron dose-dependent fluorescence in the exposed material (Lee et al., 2008; David & Barry Williams, 2010; Drobny, 2010; Sezen et al., 2011). Monitoring the sample with fluorescence microscopy during electron irradiation could shed more light on the nature and dynamics of these reactions. The bond scission and cross-linking are predominantly caused by the low-energy secondary electrons (Van Dorp, 2016) that are generated because of inelastic scattering of the higher energy primary electrons. Thus, for this purpose, it would be beneficial to be able to reduce the impinging electron energy to the few electron volts energy range of the secondary electrons, so that the contribution of a particular electron energy range could be directly studied. Alternatively, imaging with an electron beam energy below 100 eV could potentially reduce the number of secondary electrons in the sample and thus reduce sample damage.

Here, we report the implementation of an integrated fluorescence and scanning electron microscope with a retarding field for electron landing energies down to a few eV. We solely bias the sample, thus maintaining the capability of performing high numerical aperture, that is, low working distance, fluorescence microscopy without the need to entirely bias the fluorescence microscope objective lens or microscope chassis. Using a high numerical aperture lens is important as this translates to higher resolution imaging and higher photon collection efficiency. We show the energy calibration of our integrated fluorescence retarding field setup at few eV energies and provide initial examples of both contrast improvement in integrated CLEM with a retarding field, and the measurement of electron-energy-dependent fluorescence bleaching down to a few eV landing energy.

Materials and Methods

CLEM Samples

Rat pancreas tissue from a BB rat was fixed and immunolabeled as described previously (Scotuzzi et al., 2017). In brief, the tissue was fixed in 4% paraformaldehyde and 0.1% glutaraldehyde followed by a post-fixation with 1% osmiumtetroxide/1.5% potassium ferrocyanide. The tissue was embedded in EPON (SERVA). Ultra-thin (80 nm) sections were cut and collected on indium tin oxide (ITO) glass (Optics Balzers). The sections were incubated with guinea pig anti-insulin antibody (Invitrogen lot # SE2381176) followed by a biotinylated donkey anti-guinea pig secondary antibody (Jackson-IR lot # 137834) and finally a streptavidin-conjugated Alexa 594 (Jackson-IR lot # 016-580-084). Subsequently, the samples were stained with Hoechst 33258 (Sigma-Aldrich lot BCBF4593v).

Human cervical cancer epithelial (HeLa) cells transfected with GFP-C1 were high-pressure frozen, freeze substituted and embedded in HM20 resin as previously described (Peddie et al., 2014a). Serial ultra-thin sections of 100 and 50 nm thicknesses were cut from the polymerized resin blocks using a 45-degree diamond knife (Ultra Jumbo, Diatome) and collected directly on ITO-coated coverslips.

CLEM Imaging

All FM and EM imaging were conducted with an integrated microscope (Verios SEM FEI, Eindhoven, The Netherlands) equipped with an SECOM fluorescence microscope (Delmic, Delft, The Netherlands) that was modified to apply a retarding field as described in detail in the corresponding section. All further details of the microscope and its various components can also be found in that section.

FM images were acquired prior to EM to prevent bleaching by the electron beam. Hoechst and Alexa images were acquired sequentially using an excitation wavelength of, respectively, 405 and 555 nm, with a 10 s camera exposure time and using a 60× 0.7 NA long working distance objective lens (Nikon CFI S Plan Fluor ELWD 60XC).

EM images on rat pancreas samples were acquired in UHR mode with the circular backscatter detector (CBS) using a current of 0.4 nA, a dwell time of 3 μs, and 5 mm working distance. The primary beam energy was varied such that the landing energy was 1.5 keV with the applied bias. The signal on all four segments of the CBS detector was summed. Throughout the images, the gain of the detector was changed to prevent clipping of the EM signal.

EM images on HeLa cells were acquired also in UHR mode with the CBS detector, a current of 0.4 nA, pixel dwell time of 5 μs, and working distance of 5 mm, unless explicitly stated otherwise.

In all EM images, the contrast was inverted to resemble TEM-like contrast as is typical for tissue sections in biological SEM.

Fluorescence Samples and Bleaching Experiments

Microscopy cover glass slides (no. 1 thickness) coated with approximately 10 nm of ITO (Optics Balzers AG, Balzers, Liechtenstein) were used as a sample support. The ITO surface was coated with 6 nm of Al_2O_3 via atomic layer deposition to prevent quenching of the fluorescence (Moerland et al., 2016).

A 60 μM solution of tetraphenoxy-perylene diimide in toluene was then dispensed on the coated glass slide until it was fully covered and spin coated at 2,000 rpm to form a homogeneous layer.

The glass slide coated with the fluorescent dye was then fixed onto the sample carrier ring and mounted in the integrated microscope. FM excitation was done using 555 nm excitation wavelength LED source (Omicron Laserage, Rodgau-Dudenhofen, Germany) and a power of 30 mW at the sample plane. A brightline Pinkel filterset optimized for DAPI, FITC, TRITC, and Cy5 was used. Imaging was performed with a 250 ms exposure time using a Zyla 4.2 plus sCMOS camera (Oxford Instruments). For EM, a $27 \times 27\ \mu m^2$ area was scanned

with 1 keV primary electron beam energy, 13 pA current, and a 1 μs dwell time. The electron beam monochromator was used, and the stage bias was adjusted to perform experiments with landing energies ranging from 1 keV to 5 eV. Each experiment was repeated nine times per landing energy.

Results and Discussion

Retarding Field Integrated Microscope

Our main requirements for the retarding-field EM setup with an integrated fluorescence microscope are (i) high-efficiency photon detection and high optical resolution, (ii) EM-signal detection at landing energies of a few eV to calibrate the landing energy, and (iii) being able to apply high voltages without electric discharge. For the high-efficiency photon detection and light microscopy resolution, we wish to use a high numerical aperture air objective close to our sample. For EM-signal detection close to 0 eV, we require a detector above the sample that can detect high energy reflected electrons or strongly accelerated near 0 eV electrons. Finally, to prevent electric discharge, distances between biased and grounded regions should be sufficiently large to allow maximum field strengths of 5 kV/mm.

We based our microscope on a standard, commercially available SEM with an integrated fluorescence microscope. This combination is schematically illustrated in Figure 1a. The integrated microscope includes an objective lens, which is located below the sample inside the vacuum. High NA objective lenses have working distances in the range of millimeters which can lead to electric discharge between the objective and sample when subject to a strong electric field. Therefore, different objective lenses are used for different voltages. For voltages below −1 kV, we use a 0.95 NA lens, whereas for higher voltages of up to −3 kV, we use a 0.7 NA lens. The remaining optics for the excitation (green) and emission (red) pathways are located outside the vacuum of the SEM. The Verios SEM is equipped with an electron monochromator allowing low energy dispersion, which we will illustrate and characterize later. Also, the SEM is equipped with a circular backscatter (CBS) and in-column detector (ICD). The latter allows EM signal detection high up in the electron column, needed for EM-signal detection close to 0 eV. As the fields of view of both microscopes overlap, simultaneous fluorescence and electron microscopy are made possible.

To implement a negative stage bias, we modify the sample stage of the integrated microscope. A custom-made top plate is mounted to the sample stage as illustrated in Figures 1b and 1c. This top plate consists of an inner ring that is electrically insulated by PEEK screws from the rest of the stage. This makes it possible to bias the central region of the top plate instead of the entire SEM chassis and makes it safe to handle the door during an applied external high voltage. An external high voltage source (HCN 35-12500) floated by a 300 V power source (Delta Elektronica E0300-0.1) is wired to the top plate's inner and outer region using one of the SEM vacuum feedthroughs. By using a 1:10 voltage divider to measure the applied voltage, we can apply negative bias potentials with 0.1 V precision. Conductive ITO-coated glass slides (Optics Balzers) are mounted to a metal ring and clamped to the inner ring of the top plate, thus obtaining the same voltage as the top plate. The fluorescence objective lens images the sample through the central hole in the top plate. Thus, a negative stage bias
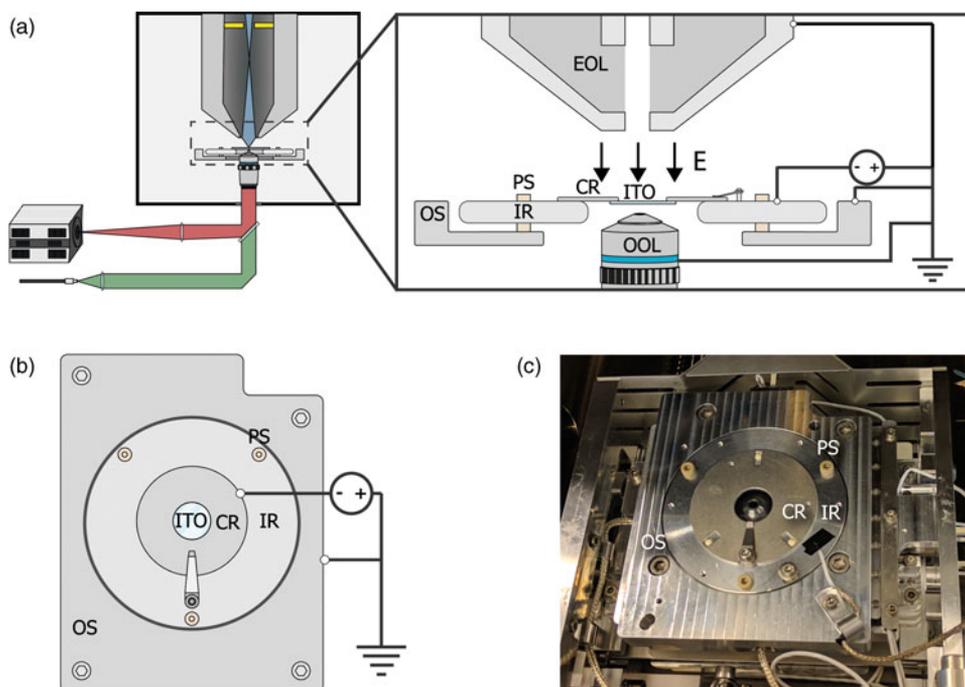

Fig. 1. (**a**) Schematic of the integrated light and electron optical microscope. Green and red indicate optical excitation and emission pathways, respectively. Blue indicates the trajectories of the primary electrons, the position of the in-column detector is indicated in yellow. Inset shows a schematic view of the sample stage. An inner ring (IR) is electrically insulated from the outer part of the sample stage (OS) by PEEK screws (PS). A negative bias is applied between the sample and electron microscope objective lens (EOL), creating a retarding electric field E. A sample is mounted on an ITO-coated glass slide (ITO), which is fixed, in electrical contact, to a sample carrier ring (CR), which clamped onto the inner ring. An optical objective lens (OOL) allows for photon excitation and detection. (**b**) Top-down view of the sample stage. (**c**) Image of the sample stage showing the location of various components named in (**b**).

can be applied while simultaneous optical imaging can be performed with high numerical aperture fluorescence objective lenses.

Electron Landing Energy Calibration

In the previous paragraph, we described how we can set the bias voltage with 0.1 V precision. However, small errors in the voltage divider may lead to deviation of the readout versus the actual set bias. Furthermore, accuracy is not only affected by the precision of our voltage sources. The ripple of the power supply, work function differences between electron source and sample, and energy spread in the electron beam can also affect the final accuracy of the electron landing energy (E_L). For higher landing energies this is not an issue, however for energies close to 0 eV these effects become significant. Therefore, we developed a method to calibrate the actual E_L and the energy spread expected in our measurements. This method is based on the reflection of the electron beam as E_L passes through zero.

For $E_L = 0$ eV, the sample acts like a mirror and electrons are reflected up into the column (Fig. 2a). The signal from scattered electrons close to 0 eV is low; however, when all primary electrons are reflected back up into the column, they will hit the ICD. Thus, we expect a steep increase in the signal on the detector when we transition from no reflection to full reflection of the beam. Figure 2b shows a series of ICD images taken with a primary beam energy of 1 keV, 25 pA current, scanning a bare ITO-glass slide with 3 μs dwell time for different stage bias values. The detector contrast and brightness were set such that neither the reflected nor the background signals were saturated. First, we see a sudden rise in the detector signal starting around −996.2 V confirming the reflection of electrons. Second, we see the appearance of several features in the images at different stage bias values, such as a central dark circle in all images, a large gray disk with a surrounding dark background at bias values

below electron reflection, and a small displaced bright cutoff disk with a barely visible grid-like pattern during electron reflection.

Both the central dark circle and the grid-like pattern are believed to be part of the solid-state detector. Since the ICD is located inside the electron column, the primary electron beam is required to pass through, which is why we observe the central hole. We believe that the grid is part of the solid-state detector possibly used to pull more electrons into the active layer, thus improving the efficiency of the detector. A dark gray disk surrounded by a dark background appears in the images before electron reflection. This is most likely due to electrons scattered from the sample that reaches the ICD. Because we used a low magnification, the electron beam gets blocked for larger scanning angles resulting in the observed pattern. This effect can also be observed in a regular SEM without any stage bias involved.

Finally, upon electron reflection we see (i) the dark gray disk disappears in the images and (ii) it is replaced by a bright cutoff disk. This cutoff disk is displaced from the image center and smaller with respect to the dark gray disk it replaced. We attribute the bright cutoff disk to the reflected electrons. Whereas scattered electrons return with various angles to the detector, upon reflection the angle is fixed. Thus, scattered electrons can move in a direction toward the optical axis, whereas reflected electrons will always move further from the optical axis than the incoming beam. Thus, while all reflected electrons might be blocked from returning in the column at certain beam angles, a fraction of the scattered electrons could still return—explaining the difference in size between the dark gray and the bright cutoff disk. The displacement of the bright disk with respect to the central hole could be due to various reasons. For one, the sample could be slightly tilted, causing the retarding field to be tilted and thus act like a tilted mirror. The location of the detector could also be responsible. The detector is located above the deflection field through which the electrons return. It could be that this deflection field alters the trajectory of returning electrons resulting
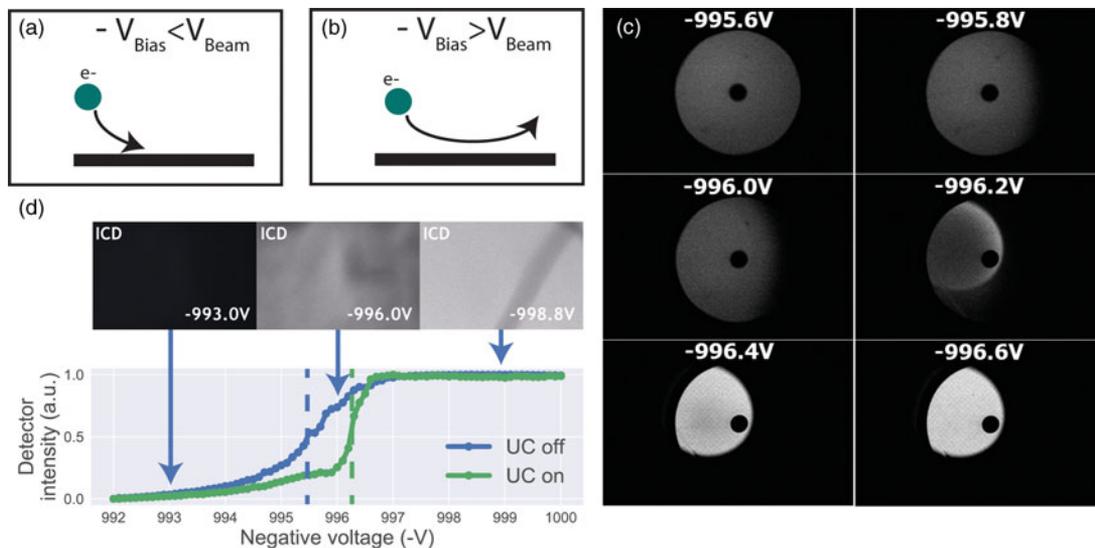

Fig. 2. (**a,b**) Illustration of our method to determine the stage potential at which the landing energy equals 0 eV. If $−V_{bias} \geq V_{beam}$, the beam will be reflected upwards causing an increase in signal for the detector high up in the electron column. (**c**) Images taken with an in-column detector with a 1 keV primary beam energy, electron beam monochromator and varying the sample stage bias such that the electron landing energies are close to 0 eV. Starting from −996.2 V, the detector signal increases caused by primary electrons being reflected into the column and consequently hitting the ICD. The central dark spot is the ICD aperture. (**d**) Average in-column detector intensity for different applied negative stage bias, with and without using the electron beam monochromator (UC). The signal increases from 0 to 1, indicating increasing reflection of the beam when the landing energy passes 0 eV. Arrows indicate the data points corresponding to the depicted images, dashed lines correspond to 50% detector intensity, taken to be $E_L = 0$.

in a shift. We note that for a full understanding, one would simulate how these electrons pass through the column. However, due to the presence of the deflection field, it would become difficult to simulate as well as interpret which electrons will hit the detector where. Moreover, for our purpose of calibrating the electron landing energy, the clear increase in signal intensity locally on the detector when the beam starts to be reflected, serves the purpose as detailed below.

By taking the average intensities of ICD images with a higher magnification and normalizing it to the maximum detector signal, an estimate energy spread in the electron beam can be obtained. We demonstrate this by performing the experiment with and without the electron beam monochromator (UC). We define the point of reflection ($E_L = 0$ eV) where the detector intensity reaches 50% full reflection. Looking at the FW50 of the signal, we extract an energy spread of 1.2 eV (UC off) and 0.3 eV (UC on), respectively. Hence, we are able to determine $E_L = 0$ eV and extract the expected energy spread in our measurements by reflecting the beam back into the column. We note that electron reflection does not occur at exactly −1 kV bias, but at a slightly lower bias value. This is due to the work function difference between the sample and the Schottky source. The energy spread both with and without UC are higher than expected for a Schottky source which can be for several reasons such as ripple of the power supply and carbon deposition during imaging. Thus, our method is not directly suitable for precisely measuring the beam's energy spread but is however appropriate for estimating the final energy spread in our measurements.

Signal Enhancement for CLEM Samples

Having established a retarding-field integrated light and electron microscope, we next illustrate its potential benefit in three applications. First, we look at imaging of biological tissue sections prepared for both fluorescence and electron microscopy. In Figure 3, EM, FM, and the CLEM overlay are shown for 80 nm rat pancreas tissue labeled with Hoechst and Alexa 594 targeting insulin. All EM images are acquired with a 1.5 keV landing energy, while the applied stage bias varies from 0 to −1 kV and the primary beam energy correspondingly from 1.5 to 2.5 kV. All other beam settings such as dwell time and beam current were kept constant. As can be expected, the stage bias does not affect the FM images. However, the implementation of the negative stage bias clearly shows an increase in CBS detector signal. Biological features, such as cell nuclei (stained with Hoechst and visible in blue in the FM images) and insulin granules (labeled with Alexa 594 and visible in orange in the FM images) can be discerned in all three EM images (Figs. 3a, 3c, 3e).

Magnified areas of insulin-rich regions further illustrate the effect of a stage bias on EM contrast. At a stage bias of 0 V (Fig. 3b), the granules are nearly indistinguishable from the background. However, by using a stage bias of −500 V (Fig. 3d), these insulin granules start to appear more clearly in the images. Increasing the bias further to −1 kV (Figs. 3k, 3f) shows that the contrast improves even further, making the insulin features crystal clear. To complement information from the visual appearance of the images, we took 10-pixel wide line profiles across insulin granules (Fig. 3g). In case of a 0 V stage bias, the noise levels are indeed too high to distinguish a feature in the line profile. We see that upon increasing the stage bias, the noise levels are reduced and that features can be recognized in the line profile. It is important to note that the noise levels appear reduced due to lowering the contrast setting of the detector itself to prevent saturation of the signal. Higher signal thus leads to lowering of the contrast and therefore the noise levels seem to be reduced while the signal strength appears to be roughly the same.

We attribute the improvements in image quality to the acceleration of electrons from the sample to the detector, since the landing energy and thus the electron interaction volume remains constant. This can lead to the visualized improvements in two ways. First, accelerated backscattered electrons hit the solid-state CBS detector with higher energy and can thus generate higher
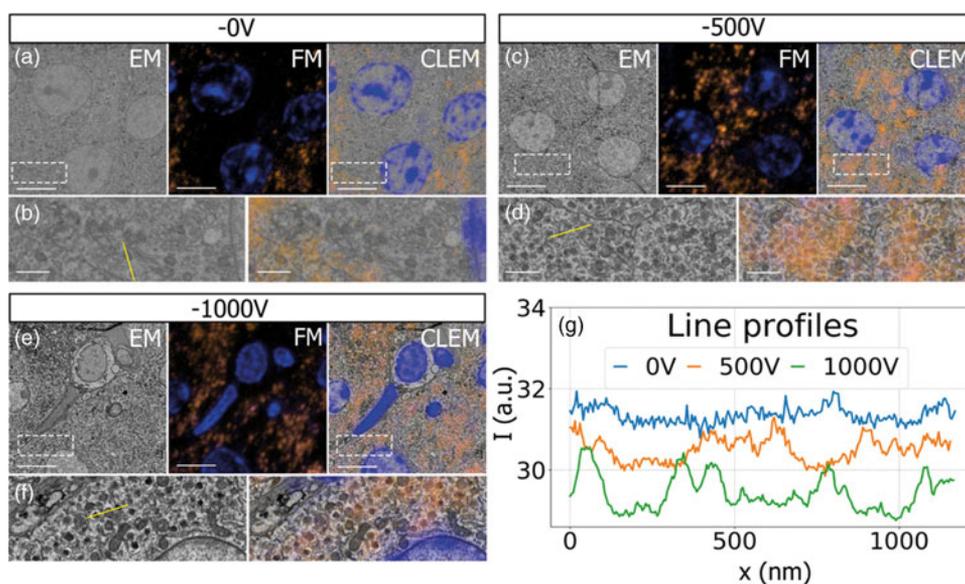

Fig. 3. EM, FM, and correlative images of 80 nm rat pancreas tissue with Hoechst (blue) and insulin (orange) labeling for increasing stage bias from 0 V (**a**), −500 V (**c**), and −1,000 V (**e**), but with a constant landing energy of 1.5 keV. Insets show EM and CLEM (**b,d,f**) magnified areas of insulin rich regions. 10-pixel wide line profiles (**g**) were taken across one or multiple insulin granules (indicated by yellow lines in the inset), plotted with an increasing offset of −1.5. Scale bars are 5 and 1 μm for, respectively, the full-scale images and insets. Increasing the negative stage bias leads to an increase in EM contrast, FM contrast remains the same.

signal per incident electron (Sakic et al., 2011). Second, the upward acceleration by the stage bias decreases the lateral spread of backscattered electrons, causing more electrons to stay within the solid angle covered by the CBS detector. In both cases, the retarding field leads to an increase in detection signal per impinging primary electron and ultimately improves the image quality of EM images.

Improved EM Signal for In-Resin Fluorescence Sections

The improvements in signal collection and image contrast for electron microscopy images can be particularly beneficial if a sample preparation protocol is followed that is aimed at preserving fluorescence already present in the sample. In this case, as opposed to the rat pancreas samples used, neither strong fixation with osmium nor the use of relatively high amounts of heavy metals for staining is possible as this would quench the fluorescence. Also, the procedures for resin embedding need to be modified to prevent full dehydration of the fluorophores, which could also lead to extraction of the hydration shell and a loss of fluorescence. To illustrate, we used a sample of HeLa cells expressing Green Fluorescent Protein (GFP), which were high-pressure frozen and embedded in HM20, following a previously published in-resin fluorescence protocol aimed at preservation of the GFP fluorescence (Peddie et al., 2014a, 2014b) such that even super-resolution localization microscopy could still be conducted (Peddie et al., 2017).

After mounting the sample in the integrated microscope, GFP signal from the sample can be clearly identified with the fluorescence microscope (Figs. 4a, 4b) at atmospheric pressure, highlighting the position of cells in the section. Recording EM images with the CBS detector with a 1.5 keV landing energy, 30 μs dwell time and the absence of a retarding field as in the example above gives a very weak signal (Fig. 4c). However, if a

retarding field of −1.5 keV is used, again with 1.5 keV landing energy (Fig. 4d), the image quality is markedly improved. Cell membranes and organelles are now much more easily visible despite a factor six lower dwell time and without any post-processing of the images. We note that the cell membranes appear patchy in the images. This is most likely caused by the cell membranes having heterogeneous uranyl acetate staining making fluorescence distribution appear "patchy." FM images were obtained before vacuum pump down. Previously, GFP fluorescence was recorded at 200 Pa in an environmental SEM (Brama et al. 2015), which is not possible in our setup and would also not be advisable while simultaneously applying a retarding field. For this reason an automated overlay was not possible, and instead, the fluorescence overlay on the −1.5 kV stage bias EM image is done manually (Figs. 4e, 4f). The EM images with a retarding field demonstrate, like the pancreas sections, that the signal in the EM images improves by the retarding field. One could even argue that the improvement appears to be stronger compared to the pancreas sections as features of the HeLa cells without a stage bias are hard to distinguish by eye. Based on these results, we can conclude that a retarding field improves the EM signal for different types of sample preparation. Hence, the use of a retarding field could provide a way to image samples that under normal circumstances do not generate a sufficient amount of EM signal.

Landing Energy Optimization for Ultra-thin Sections

The application of a retarding field in an SEM not only allows for improved contrast but also enables imaging of very thin sections by fine tuning the electron landing energy in the low or sub-keV range. Reducing section thickness is important especially when serial sections are considered for the process of volume reconstruction of a sample—sometimes also referred to as array tomography. The section thickness then directly translates to the resolution in the third (out-of-plane) dimension, which for a correlative experiment is then equal in FM and EM. Using super-resolution fluorescence microscopy, lateral FM localization accuracy of 80 nm for the in-resin fluorescence sample described previously has been demonstrated (Peddie et al., 2017). Decreasing section thickness would decrease the amount of fluorophores and, thus, increase their sparsity which will ultimately result in a higher FM resolution. Simultaneously, a reduced section thickness will improve the axial resolution. Achieving a 50 nm isotropic FM resolution would come close to rivaling the resolution of immunolabeling with primary and secondary antibodies and a gold particle (Kopek et al., 2012). However, EM imaging of 50 nm sections has so far remained a daunting task due to a lack of EM signal even at higher dwell times. Here, we used these 50 nm sections of HeLa cells in HM20 to show the benefit of landing energy optimization for very thin sections.

The CBS detector used in each of our CLEM experiments is inserted below the SEM polepiece (Fig. 5a) and consists of four ring segments—labeled A through D as indicated in Figure 5b. Without a stage bias, these respective ring segments correspond to scattering angles of 163°–152°, 152°–140°, 140°–130°, and 130°–122°. While in the previous results, the signal over all four segments was summed, in the following we will use the different rings to distinguish between electron scattering angles and therefore different types of EM signals. To prevent saturation of the signal, the detector's brightness was adjusted
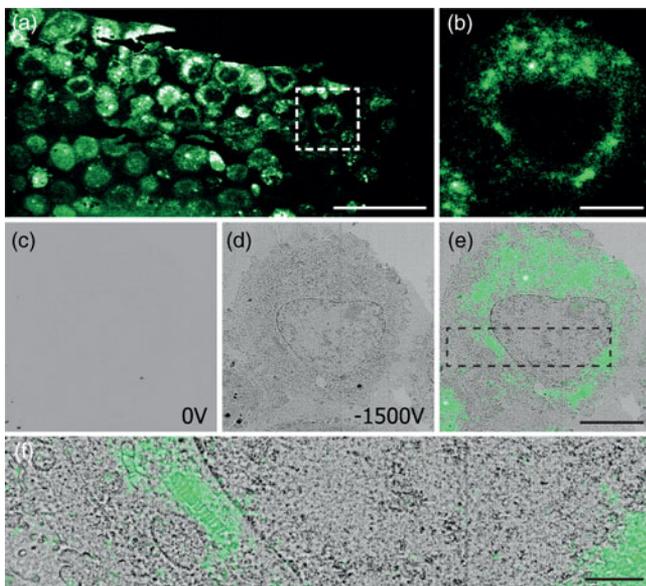
Fig. 4. Correlative images of in-resin embedded 100 nm HeLa cell sections labeled with GFP, (**a,b**) FM images in ambient conditions. (**c,d**) EM images using a 1.5 keV landing energy and (**c**) 0 V stage bias and 30 μs dwell time, (**d**) −1.5 kV stage bias, and 5 μs dwell time. (**e,f**) Manual correlative overlay. Scale bars: (**a**) 50 μm, (**b–e**) 10 μm, (**f**) 3 μm.
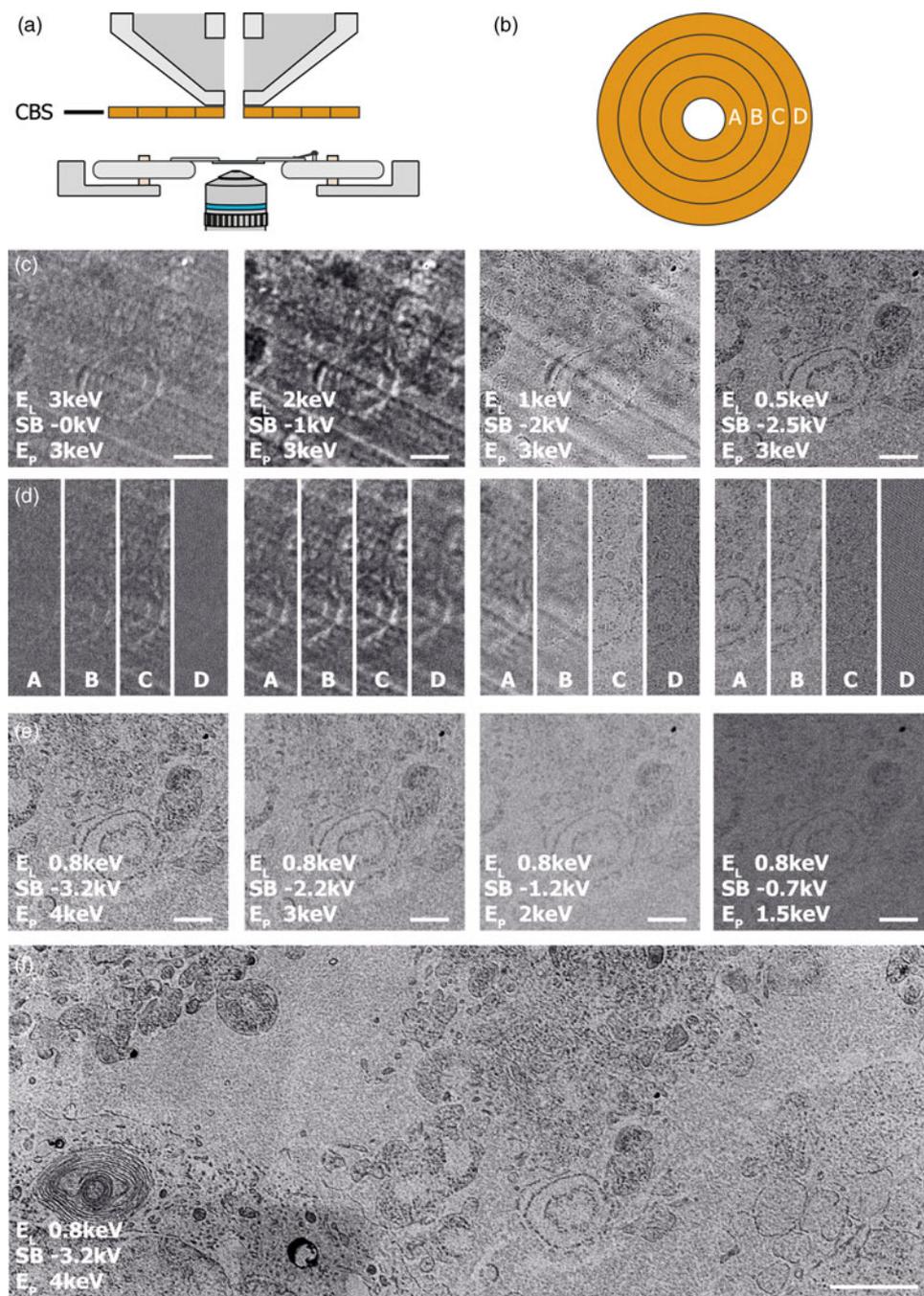
Fig. 5. (**a**) Illustration of the insertable CBS-detector located directly below the SEM polepiece. (**b**) The CBS consists of four rings which allow separate detection per ring, labeled as A, B, C, and D. EM images of 50 nm sections of HeLa cells were obtained using the CBS detector, a current of 400 pA, a 5 μs dwell time, and various E_P, stage bias (SB) and E_L. (**c**) EM images E_P = 3 keV and E_L ranging from 3 to 0.5 keV. At lower E_L cellular features appear sharper and sample topology disappears. (**d**) Contributions of the individual CBS rings to the EM images in (**c**). Lowering E_L creates the possibility to discern between sample topology and cellular features. Furthermore, lowering E_L leads to the signal moving to the central rings. (**e**) EM images for E_P ranging from 4 to 1.5 keV but constant E_L using CBS ring A and B only. Contrast reduces by reducing SB but features in the image remain unchanged. (**f**) Large FOV image for E_P = 4 keV and E_L = 0.8 keV using ring A and B only. Scale bars are 1 μm in (**c–e**) and 2 μm in (**f**).

throughout the images, while the contrast setting remained the same.

The EM signal changes and improves by lowering E_L for the 50 nm sections as expected. EM images of these sections were taken using a primary beam energy of 3 keV and retarding field strengths of 0 V to −2.5 kV, leading to electron landing energies of 3–0.5 keV (Fig. 5c). The EM image at E_L = 3 keV shows numerous

effects. First, the EM contrast appears to be weak, suggesting that the EM signal is weak as well. Second, we recognize features by a bright outline in the image in stark contrast to all results shown so far. Since the penetration depth at 3 keV is expected to be larger than the 50 nm section thickness (Bouwer et al., 2017; He et al., 2018), this could be caused by the electron beam fully penetrating the section combined with strong scattering on the ITO substrate

below. This would effectively give rise to a transmission-like contrast (Pluk et al., 2009). Finally, we see unidirectional stripes pointing diagonally in the image, most likely these would originate from marks on the diamond knife leading to scratches in the sample that point in the direction of the cut.

Increasing the stage bias to −1 kV, thus lowering E_L to 2 keV, we see that the contrast in the images improves. Yet, both the stripe pattern and the bright appearance of cellular features persist. Further lowering E_L to 1 keV reveals a striking change in the EM image as feature contrast in the images now inverts. Finally, at 0.5 keV, landing energy the stripe pattern also disappears from the images and the image and feature appearance is similar to that observed for the thicker sections in Figure 4. Thus, we see that the ability to tune the landing energy to the sub-keV domain drastically improves contrast for ultra-thin sections and for detection with the CBS detector also removes the appearance of sectioning artifacts.

We next identify the contribution of the individual segments of the CBS detector to the images for each E_L from Figure 5c. Figure 5d shows images of the same area for each individual detector ring for E_L ranging from 3 to 0.5 keV. For each E_L, we can identify different contributions to these detector rings. At $E_L = 3$ keV, we observe an overall weak signal and contrast. Furthermore, we can see that most of the signal is detected on rings B and C. Lowering to $E_L = 2$ keV causes an overall increase in signal, likely due to acceleration of electrons to the detector. Despite the acceleration of the electrons, causing their lateral spread to be narrowed, we see that most of the signal still appears on rings B and C. At $E_L = 1$ keV, we can recognize different effects taking place on the different detector segments. First, we see the contrast of the cellular features invert on all segments compared to the images obtained at higher landing energies. However, on both rings A and B, a slight bright outline around these features seems to be present. Second, the striped pattern caused by the cutting-induced surface topography is absent on rings C and D. Finally, for $E_L = 0.5$ keV, we see that this surface topography is absent on all rings. Furthermore, we see that at this energy most of the signal appears on ring A and B. Thus, the signal has moved radially inwards with respect to $E_L = 1$ keV. The images of rings C and D consist mostly of noise. Therefore, to reduce the noise in images at $E_L = 0.5$ keV, imaging should be preferably performed only with rings A and B.

Using this information, we can look for optimized conditions for acquiring EM images of the 50 nm sections. By varying E_L between 1 and 0.5 keV, we found the best setting to be at 0.8 keV. Similar to Figure 5d with $E_L = 0.5$ keV, most of the signal appears on rings A and B, while rings C and D mostly contribute noise. Figure 5e shows images obtained at $E_L = 0.8$ keV with primary beam energy varying from 4 to 1.5 keV. At a constant E_L but increasing stage bias, we see that the contrast in the images keeps improving. Thus, the optimal setting appears to be at a primary beam energy of 4 keV with a −3.2 kV stage bias. Figure 5f shows the larger area acquisition obtained with these parameters. If we further compare the image series in Figure 5e with the other results, we see with constant E_L but different retarding field strength that (i) the type of contrast between features in the image remains the same and (ii) the striped patterns do not appear even at lower retarding field strength. Thus, the changing visibility of surface topography features and the inversion of contrast of the features of interest in the image are not related to the strength of the retarding field but rather to the landing energy. Therefore, we can conclude that these changes in contrast of

the surface topography features are not caused by collimation of either the secondary or backscattered electrons due to the upward acceleration of the retarding field.

Several factors may play a role in the signal dependency on landing energy. First, it should be noted that the sample is highly heterogeneous with a complicated surface morphology. Topographic features, such as the cutting artifacts, are clearly visible in several of the images. In addition, in the composition, stained material alternates with native biological material and a particularly soft embedding polymer, namely acrylic HM20. Besides density differences, this may also give rise to additional height variations at smaller typical length scales than the cutting artifacts. In Figure 5c, at 2 and 1 keV landing energy, contrast inversions around stained features can indeed be observed, pointing to an apparent topography contrast in the images. The landing energy dependence may then come into play via the axial and lateral extent of the interaction volume: if these decrease and become smaller than the typical length scales involved in the surface topography, the topography contrast may disappear from the images, in correspondence with our results. Note that the presence of conductively stained material and insulating polymer may also give rise to a varying electric field distribution. However, we exclude this as a contributing factor to the observed contrast differences as there is only a landing energy and no retarding-field dependency.

Penetration of the primary electron beam through the section material could give rise to contrast inversion, as the strong scattering of electrons on the underlying ITO substrate may give rise to transmission contrast. For landing energies above 2 keV, the estimated penetration depth of the electrons would be larger than the on average 50 nm section thickness. For our optimal landing energy, $E_L = 0.8$ keV, 12 nm would be a reasonable estimate (He et al., 2018). However, the thickness may vary within the section, for example, due to the cutting artifacts, and the material density may vary locally, for example, due to a low polymer filling fraction, and compression of material during cutting. Another factor that could influence the observed contrast inversion when decreasing the landing energy, could be the variation in electron scattering yield going from higher than 1 to lower than 1. This combined with variation of sample composition of stained, biological, and soft polymer material on a microscopic level could lead to an inversion of contrast of certain features. More research, with well-characterized, thin samples, and backed by electron scattering and ray-tracing calculations, should be conducted in order to obtain a better understanding of the observed variations in image quality and contrast with landing energy. Lastly, we note that the observations of the segmented detector (Fig. 5d) suggest that electrons exiting the sample under a relatively large angle with respect to the surface normal are least affected by the processes responsible for these variations.

Direct Visualization of Electron-Induced Bleaching

As a third example application of our retarding-field integrated microscope, we show the direct visualization of electron-induced bleaching of fluorescent molecules. To this end, perylene diimide fluorescent molecules are used as a model system. The fluorescent dye is spin coated from a dilute solution to form a homogeneous, thin layer on an alumina-ITO-coated glass slide. The slide is mounted in the integrated microscope and we then monitor the bleaching of the fluorescent dye due to electron irradiation according to the scheme indicated in Figure 6a: first, an FM
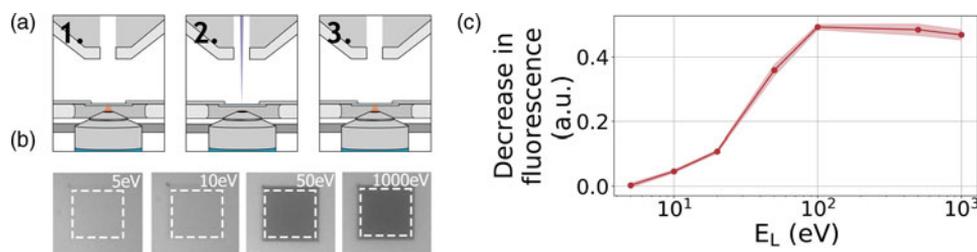
Fig. 6. (**a**) Acquisition method for determining electron beam induced damage by fluorescence bleaching. (1) An FM image is taken after which (2) an area of 27 × 27 μm^2 is scanned by the electron beam of a certain landing energy. (3) After scanning an FM image is taken. (**b**) Resulting final FM images for various electron landing energies. Decreasing the electron landing energy results in a decreasing amount of bleaching. (**c**) Relative decrease in fluorescence after electron irradiation for landing energies from 1 kV to 5 eV.

image is taken, then an area within the FM field of view is scanned with the electron beam, and finally, an FM image is taken directly after scanning to record the bleaching induced by the electron beam. We conduct this procedure several times with a fixed dose for different E_L.

A decrease in fluorescence bleaching is observed by reducing the electron landing energy. In Figure 6b, we show our FM images taken after the electron irradiation for landing energies of 1 keV, 50 eV, 10 eV, and 5 eV. The irradiated regions can be easily distinguished as these appear darker with respect to non-irradiated regions. This is due to the electron-induced bleaching of the fluorescent molecules, causing the exposed areas to emit less fluorescence. Also, we can see that there is a decrease in the bleaching when the landing energy is reduced. This effect is especially pronounced upon going from 50 to 10 eV as the exposed area appears brighter for the latter energy. In Figure 6c, we show the relative decrease in fluorescence after the electron irradiation for the different landing energies. Each data point is averaged over nine measurements. Starting with energies ranging from 1 keV to 100 eV, we see that there is no significant change in the fluorescence bleaching due to electron irradiation. We note that the major contribution to the observed degradation of molecular fluorescence comes from low-energy secondary electrons (SEs) (Van Dorp, 2016). Reducing the electron landing energy from 1 keV to 100 eV does not alter the molecular degradation processes induced by SEs. However, upon decreasing the landing energy from 100 to 50 eV, we see that the fluorescence bleaching starts to decrease. In this regime, some molecular degradation pathways induced by SEs may become less accessible. Reducing the landing energy further to 20 eV reduces the observed bleaching to only 20%, further to 10% at 10 eV and finally only 4% at 5 eV. This means that at 5 eV, the bleaching is 12.5× less compared to beam energies of 100 eV to 1 keV. To our knowledge, this constitutes the first direct visualization of the energy-dependent electron-induced degradation in a film of organic molecules, where in addition we vary the electron energy over orders of magnitude down to only a few eV.

Several effects related to the fact that the primary beam energy approaches and then enters the typical SE energy range can contribute to this decrease. First, when the primary beam energy decreases below 100 eV, the number of generated SEs is reduced and their energy distribution is altered leading to a reduced amount of damage. Second, the penetration depth of the beam changes for different landing energies and is unknown for energies in the range of a few eV (Seah & Dench, 1979). A reduced penetration depth leads to a reduced number of bleached fluorophores as well or, since the dye layer is very thin, the reduced

penetration depth could increase the number of events in the dye layer. This would instead give rise to more bleaching at the lower energies. Third, different electron-induced damage processes can occur which may have a different range of energies in which they occur. For example, in organic molecules, direct impact ionization typically halts at about 10 eV, while dissociative electron attachment events can occur even when close to 0 eV (Van Dorp, 2016). Thus, when we decrease the electron landing energy from 20 to 10 eV and further to 5 eV, several of these pathways may be gradually switched off, leading to a decrease in the observed damage and thus bleaching. The proposed scheme of using molecular fluorescence to report on the observed damage for specific electron landing energies may provide a new avenue to study these processes *in situ*.

Outlook and Discussion

In this paper, we presented a retarding-field integrated microscope, which allows fluorescence microscopy with high numerical aperture objectives. The design only requires the user to exchange the top plate of the integrated microscope's sample stage, after which samples can be mounted to a carrier ring and be subjected to a retarding field. The top plate is electrically isolated with the rest of the stage, making the sample stage grounded and thus the entire SEM door as well. Therefore, the SEM is safe to operate during the applied biases of several kilovolts. To prevent electric discharge, we limit the bias potential to −1 kV for a 0.95 NA objective lens, while biases up to −3 kV can be achieved via an extra-long working distance 0.7 NA objective. The range of possible bias potentials is, therefore, comparable to setups in other studies used for optimized electron interaction volume and signal collection (Ohta et al., 2012; Bouwer et al., 2017).

Our demonstrated method of detecting reflected electrons up in the column by use of an ICD, a standard asset in an SEM nowadays, allows us to calibrate a zero landing energy. This method, combined with a monochromator, allows us to detect an energy dispersion of 0.3 eV, while still retaining a current in the beam. The energy dispersion here is higher than the dispersion expected from the monochromator. However, other effects such as voltage source ripple and carbon deposition during our image acquisition are expected to increase the measured energy spread further. Thus, our method of calibration does not directly represent the energy spread, but instead is a representation of the expected spread in landing energy during our experiments. More elaborate monochromators are used in TEM, but for SEM, these would require a redesign of the entire microscope. Besides that, using such types of monochromators sacrifices beam current leading

to longer acquisition times to achieve the same amount of signal. Furthermore, the measured 0.3 eV energy spread is sufficient for the application examples presented here.

The use of very low energy electrons for imaging has been mostly explored in dedicated microscopes, so-called low energy electron microscopy (LEEM) (Tromp & Reuter, 1993; Bauer, 2014). In LEEM, the electron beam energy is also reduced by implementing a retarding field between the sample and objective lens. Next, the signal beam is separated from the primary beam by a beam separator and used to reconstruct an image at energies of a few to tens of eV. Due to this beam separator, LEEM setups can be quite complicated. Alternatively, low energy electron microscopy can also be performed in an SEM by tuning the retarding field appropriately. This has been referred to as Scanning LEEM (or SLEEM) (Müllerová & Frank, 1993). SLEEM does not require the use of a beam separator, making it easier to implement. Our setup with the current detector configuration and landing energy calibration should be able, like SLEEM, to image at these very low energies. We note that such a tool could never obtain the quality of a dedicated LEEM. However, it could be used as a tool for quick inspection of surface properties of materials (Frank et al., 2011).

One application example was that the retarding-field bias leads to improved SNR and contrast-to-noise ratio (CNR) in imaging thin biological tissue sections. This is particularly beneficial for CLEM and integrated CLEM as staining and contrasting agents are typically used less in sample preparation to preserve fluorescence (Watanabe et al., 2011). We have mentioned that the retarding field could enhance the signal in two possible ways. Namely, first, by acceleration of electrons to the detector leading to an increase in detected signal per electron, and second, by decreasing the lateral spread of backscattered electrons leading to more electrons hitting the detector. A third possible way in which the signal could be enhanced, but which we did not observe in our experiments, would be via low-energy (0–20 eV) SEs hitting the CBS detector. For our flat tissue sections, these electrons will only contain information if they are generated by backscattered electrons on their way out of the sample, and thus, a large portion of these only contributes to the background signal. With a stage bias of a few hundred Volts or more, these secondary electrons will mostly be accelerated straight up into the electron column, through the CBS aperture, leading to a reduction of background in the images. Under different circumstances, such as whole cells, samples with more topography or different SEM configurations, this effect could play a role. Further research, both experimentally and via ray-tracing simulations could be directed at evaluating the stage bias and landing energy for optimal SNR and CNR. This could not only benefit CLEM, but EM on tissue in general and large-scale EM in particular as the latter could allow shorter dwell times for the same SNR/CNR and thus a higher throughput (Micheva & Smith, 2007; Wacker & Schroeder, 2013; Lane et al., 2020).

In our second application example, we showed that a retarding field can be used to improve the image quality of very thin sections by reducing the electron landing energy below 1 keV while simultaneously increasing the signal on the detector. This can be utilized in serial-section electron microscopy, where going to thinner sections also results in a higher resolution in z of the reconstructed final image. Going to lower electron landing energies leads to a smaller penetration depth of the electron probe and creates the opportunity to measure from shallower surfaces. However, imaging at lower landing energies typically leads to a weak signal. This means that imaging at energies below 1 keV

landing energies creates images with low contrast. However, we showed that for increasing retarding field strengths the contrast improves. Thus, images at landing energies far below 1 keV can be obtained with a sufficiently strong retarding field. This can be used to improve the resolution in z further for deconvolution-based subsurface reconstruction algorithms (Boughorbel, 2012; De Goede et al., 2017). Typically, EM images at energies between 3 and 0.8 keV are fed to the algorithm through which images have been reconstructed with a z-resolution of ∼12 nm (He et al., 2018). Lowering E_L further, while still retaining signal using a retarding field, creates the potential to image at resolutions of a few nanometers.

Another application example of the retarding-field integrated microscope was the direct visualization of electron-induced bleaching of fluorescent molecules. By reducing the landing energy below 100 eV, we have shown that the bleaching of fluorescent molecules also gradually decreases. We mentioned several effects that play a role in this reduction: a reduction in the number of SEs generated at lower beam energy, a changing penetration depth of the electron beam, and relative changes in the population of different electron energy-dependent molecular degradation pathways. Ultimately, at only a few eV landing energy, only dissociative electron attachment will be available as a degradation pathway, while all other pathways will be completely switched off. Further research should be directed at distinguishing these different effects so that the observed effects could be quantified in terms of molecular processes. Here, other characteristics of the measured fluorescence could open new possibilities, such as dynamic measurements as well as measuring fluorescence lifetimes or spectral shifts. Such measurements are only possible in an integrated correlative retarding field setup as presented here. This could be particularly interesting for the investigation of electron–molecule interactions where typically only fragmentation products are detected and most of the internal dynamics are obscured. Furthermore, in this field, most studies are performed on molecules in the gas phase or on clusters (Ingólfsson, 2019). Obtaining information about the processes in organic films or in solid materials could give new insights in electron–molecule interactions.

We finally note that the energy range in which we observed reduced bleaching (<100 eV) is still about an order of magnitude smaller than the optimum range found for imaging biological sections (0.8–1.5 keV). While imaging under conditions of reduced bleaching could be interesting for correlative microscopy, especially in combination with volume EM, high-resolution imaging at such low electron energies is only possible with a dedicated LEEM instrument as discussed above. Thus, we see the most direct application of this part of our research in the study of electron-induced reactions in organic or solid materials. Ultimately, this could also shed more light on the origin of beam damage in the electron microscope and thus lead to novel methods for imaging beam-sensitive materials such as biological specimen.

Conclusion

We have presented an integrated fluorescence and scanning electron microscope with the possibility to apply a retarding field between sample and electron objective lens. This allows us to reach electron landing energies of only a few eV with an accuracy of 0.3 eV, which was determined by monitoring the reflection of the electron beam up into the column onto an in-column

detector. The retarding field is beneficial for imaging samples prepared for correlative fluorescence and electron microscopy, where it allows significant contrast enhancement for samples that are weakly stained in order to preserve fluorescence. Also, tuning both landing energy and retarding field allows the user to optimize imaging conditions to section thickness which is particularly beneficial for ultra-thin sections. We finally presented a first demonstration of how our setup can be used to investigate electron beam induced damage *in situ* for electron energies down to a few eV. Further development of this approach may shed light on electron–molecule interactions in the few eV energy regime, the typical range for electrons generated in a sample through inelastic collisions.

References

Agronskaia AV, Valentijn JA, van Driel LF, Schneijdenberg CTWM, Humbel BM, van Bergen en Henegouwen PMP, Verkleij AJ, Koster AJ & Gerritsen HC (2008). Integrated fluorescence and transmission electron microscopy. *J Struct Biol* **164**, 183–189.

Ando T, Bhamidimarri SP, Brending N, Colin-York H, Collinson L, De Jonge N, De Pablo PJ, Debroye E, Eggeling C, Franck C, Fritzsche M, Gerritsen H, Giepmans BNG, Grunewald K, Hofkens J, Hoogenboom JP, Janssen KPF, Kaufmann R, Klumperman J, Kurniawan N, Kusch J, Liv N, Parekh V, Peckys DB, Rehfeldt F, Reutens DC, Roeffaers MBJ, Salditt T, Schaap IAT, Schwarz US, Verkade P, Vogel MW, Wagner R, Winterhalter M, Yuan H & Zifarelli G (2018). The 2018 correlative microscopy techniques roadmap. *J Phys D: Appl Phys* **51**, 443001.

Bauer E (2014). *Surface Microscopy with Low Energy Electrons*, vol. **23**. New York, NY: Springer.

Bischak CG, Hetherington CL, Wang Z, Precht JT, Kaz DM, Schlom DG & Ginsberg NS (2015). Cathodoluminescence-activated nanoimaging: Noninvasive near-field optical microscopy in an electron microscope. *Nano Lett* **15**, 3383–3390.

Boughorbel F (2012). *Generation of depth map for an image.* Google Patents.

Bouwer JC, Deerinck TJ, Bushong E, Astakhov V, Ramachandra R, Peltier ST & Ellisman MH (2017). Deceleration of probe beam by stage bias potential improves resolution of serial block-face scanning electron microscopic images. *Adv Struct Chem Imaging* **2**, 11.

Brama Elisabeth, Peddie Christopher J, Jones Martin L, Domar Marie-Charlotte, Snetkov Xenia, Way Michael, Larijani Banafshe & Collinson Lucy M. (2015). Standard fluorescent proteins as dual-modality probes for correlative experiments in an integrated light and electron microscope. *Journal of Chemical Biology* **8**, 179–188

David B & Barry Williams C (2010). *Transmission Electron Microscopy: A Textbook for Materials Science*, vol. **16**. New York: Springer.

De Boer P, Hoogenboom JP & Giepmans BNG (2015). Correlated light and electron microscopy: Ultrastructure lights up!. *Nat Methods* **12**, 503.

De Goede M, Johlin E, Sciacca B, Boughorbel F & Garnett EC (2017). 3D multi-energy deconvolution electron microscopy. *Nanoscale* **9**, 684–689.

Drobny JG (2010). *Radiation Technology for Polymers*. Boca Raton, Florida: CRC Press.

Frank L, Hovorka M, Konvalina I, Mikmeková Š & Müllerová I (2011). Very low energy scanning electron microscopy. *Nucl Instrum Meth Phys Res A* **645**, 46–54.

Garming MWH, Weppelman IGC, De Boer P, Martínez FP, Schirhagl R, Hoogenboom JP & Moerland RJ (2017). Nanoparticle discrimination based on wavelength and lifetime-multiplexed cathodoluminescence microscopy. *Nanoscale* **9**, 12727–12734.

He Q, Hsueh M, Zhang G, Joy DC & Leapman RD (2018). Biological serial block face scanning electron microscopy at improved z-resolution based on Monte Carlo model. *Sci Rep* **8**, 1–13.

Ingólfsson O (2019). *Low-Energy Electrons: Fundamentals and Applications*. Boca Raton, Florida: CRC Press.

Karreman MA, Agronskaia AV, van Donselaar EG, Vocking K, Fereidouni F, Humbel BM, Theo Verrips C, Verkleij AJ & Gerritsen HC (2012). Optimizing immuno-labeling for correlative fluorescence and electron microscopy on a single specimen. *J Struct Biol* **180**, 382–386.

Karreman MA, Agronskaia AV, Verkleij AJ, Cremers FFM, Gerritsen HC & Humbel BM (2009). Discovery of a new RNA-containing nuclear structure in UVC-induced apoptotic cells by integrated laser electron microscopy. *Biol Cell* **101**, 287–299.

Kopek BG, Shtengel G, Shan Xu C, Clayton DA & Hess HF (2012). Correlative 3D superresolution fluorescence and electron microscopy reveal the relationship of mitochondrial nucleoids to membranes. *Proc Natl Acad Sci USA* **109**, 6136–6141.

Lane R, Vos Y, Wolters AH, van Kessel L, Giepmans BN & Hoogenboom JP (2020). Optimization of negative stage bias potential for faster imaging in large-scale electron microscopy. *bioRxiv*.

Lee HM, Kim YN, Kim BH, Kim SO & Cho SO (2008). Fabrication of luminescent nanoarchitectures by electron irradiation of polystyrene. *Adv Mater* **20**, 2094–2098.

Liv N, Christiaan Zonnevylle A, Narvaez AC, Effting APJ, Voorneveld PW, Lucas MS, Hardwick JC, Wepf RA, Kruit P & Hoogenboom JP (2013). Simultaneous correlative scanning electron and high-NA fluorescence microscopy. *PLoS ONE* **8**(2).

Liv N, van Oosten Slingeland DSB, Baudoin J-P, Kruit P, Piston DW & Hoogenboom JP (2016). Electron microscopy of living cells during in situ fluorescence microscopy. *ACS Nano* **10**, 265–273.

Micheva KD & Smith SJ (2007). Array tomography: A new tool for imaging the molecular architecture and ultrastructure of neural circuits. *Neuron* **55**, 25–36.

Moerland RJ, Weppelman IGC, Garming MWH, Kruit P & Hoogenboom JP (2016). Time-resolved cathodoluminescence microscopy with subnanosecond beam blanking for direct evaluation of the local density of states. *Opt Express* **24**, 24760–24772.

Müllerová I & Frank L (1993). Very low energy microscopy in commercial SEMs. *Scanning* **15**, 193–201.

Müllerová I & Frank L (1994). Use of cathode lens in scanning electron microscope for low voltage applications. *Microchim Acta* **114**, 389–396.

Nagayama K, Onuma T, Ueno R, Tamehiro K & Minoda H (2016). Cathodoluminescence and electron-induced fluorescence enhancement of enhanced green fluorescent protein. *J Phys Chem B* **120**, 1169–1174.

Narváez AC, Weppelman IGC, Moerland RJ, Hoogenboom JP & Kruit P (2014). Confocal filtering in cathodoluminescence microscopy of nanostructures. *Appl Phys Lett* **104**, 251121.

Nawa Y, Inami W, Lin S, Kawata Y, Terakawa S, Fang C-Y & Chang H-C (2014). Multi-color imaging of fluorescent nanodiamonds in living HeLa cells using direct electron-beam excitation. *ChemPhysChem* **15**, 721–726.

Ohta K, Sadayama S, Togo A, Higashi R, Tanoue R & Nakamura K-i (2012). Beam deceleration for block-face scanning electron microscopy of embedded biological tissue. *Micron* **43**, 612–620.

Peddie CJ, Blight K, Wilson E, Melia C, Marrison J, Carzaniga R, Domart M-C, O'Toole P, Larijani B & Collinson LM (2014*a*). Correlative and integrated light and electron microscopy of in-resin GFP fluorescence, used to localise diacylglycerol in mammalian cells. *Ultramicroscopy* **143**, 3–14.

Peddie CJ, Domart M-C, Snetkov X, O'Toole P, Larijani B, Way M, Cox S & Collinson LM (2017). Correlative super-resolution fluorescence and electron microscopy using conventional fluorescent proteins in vacuo. *J Struct Biol* **199**, 120–131.

Peddie CJ, Liv N, Hoogenboom JP & Collinson LM (2014*b*). Integrated light and scanning electron microscopy of GFP-expressing cells. *Methods Cell Biol* **124**, 363–389.

Pinotsi D, Rodighiero S, Campioni S & Csucs G (2019). An easy path for correlative electron and super-resolution light microscopy. *Sci Rep* **9**, 1–9.

Pluk H, Stokes DJ, Lich B, Wieringa B & Fransen J (2009). Advantages of indium–tin oxide-coated glass slides in correlative scanning electron microscopy applications of uncoated cultured cells. *J Microsc* **233**, 353–363.

Sakic A, Nanver LK, van Veen G, Kooijman K, Vogelsang P, Scholtes TLM, De Boer W, *et al.* (2011). Solid-state backscattered-electron detector for sub-keV imaging in scanning electron microscopy. *Proceedings ICT. Open: Micro Technology and Micro Devices SAFE 2011*, Veldhoven, 14–15 November 2011, pp. 1–4 (Technology Foundation STW).

Scotuzzi Marijke, Kuipers Jeroen, Wensveen Dasha I, de Boer Pascal, Hagen Kees C W, Hoogenboom Jacob P & Giepmans Ben N G (2017). Multi-color electron microscopy by element-guided identification of cells, organelles and molecules. *Scientific reports* **7**(1), 1–8

Seah MP & Dench WA (1979). Quantitative electron spectroscopy of surfaces: A standard data base for electron inelastic mean free paths in solids. *Surf Interface Anal* **1**, 2–11.

Sezen M, Plank H, Fisslthaler E, Chernev B, Zankel A, Tchernychova E, Blümel A, List EJW, Grogger W & Pölt P (2011). An investigation on focused electron/ion beam induced degradation mechanisms of conjugated polymers. *Phys Chem Chem Phys* **13**, 20235–20240.

Timmermans FJ & Otto C (2015). Contributed review: Review of integrated correlative light and electron microscopy. *Rev Sci Instrum* **86**, 011501.

Tromp RM & Reuter MC (1993). Imaging with a low-energy electron microscope. *Ultramicroscopy* **50**, 171–178.

Van Dorp WF (2016). Theory: Electron-induced chemistry. *Front Nanosci* **11**, 115–133.

Wacker I & Schroeder RR (2013). Array tomography. *J Microsc* **252**, 93–99.

Watanabe S, Punge A, Hollopeter G, Willig KI, Hobson RJ, Wayne Davis M, Hell SW & Jorgensen EM (2011). Protein localization in electron micrographs using fluorescence nanoscopy. *Nat Methods* **8**, 80.

Yuan H, Debroye E, Janssen K, Naiki H, Steuwe C, Lu G, Moris M, *et al.* (2016). Degradation of methylammonium lead iodide perovskite structures through light and electron beam driven ion migration. *J Phys Chem Lett* **7**, 561–566.